

Active control the peak value of Hanbury Brown-Twiss effect with classical light by holographic projection

Liming Li,* Xueying Wu, and Gongxiang Wei

*School of Physics and Optoelectronic Engineering,
Shandong University of Technology, Zibo 255049, China*

(Dated: October 24, 2025)

The Manipulation of $g^{(2)}(0)$ peak value of Hanbury Brown-Twiss (HBT) effect is discussed with a holographic projection scheme. By the aid of target pattern artificially designed in the projection imaging system, the statistical distribution of projection pattern will be highly controllable. In this work, we theoretically point out key factors influencing the $g^{(2)}(0)$ peak value of HBT effect in a single-lens incoherent imaging system. We find the peak value is not only decided by statistical property and coherence length of target pattern but also depends on the intrinsic characteristics of projection system, such as numerical aperture and projection quality. Then, we experimentally measured the $g^{(2)}(0)$ peak value of HBT effect with a phase-only holographic projection scheme and demonstrate the applicability of our theoretical analysis on the holographic scheme. Here, the super-bunching effect in the projection plane has been observed, when target patterns originated from chaotic speckle or it's function transformation patterns. Moreover, we design some sparse target patterns, whose holographic reconstruction patterns show the super-bunching effect achieving $g^{(2)}(0) = 39.77$. Finally, we discussed the positive influence of holographic noise on increasing the $g^{(2)}(0)$ peak value. The presented work predicting the peak value of HBT effect not only is applicable for the lens imaging system but also in other projection systems, such as the holographic projection.

I. INTRODUCTION

People have rediscover the photon interference since the Hanbury Brown-Twiss (HBT) effect was discovered in 1956 [1, 2]. The intensity correlation was adopted in the experimental detection strategy. Until then, the conventional wisdom hold that the intensity detection inevitably discards the phase information leading to precluding the phenomenon of photon interference [3, 4]. However, the HBT effect breaks this inherent understanding and pushes a new concept, i.e., multi-photon interference, to researchers [5–7]. According to the two-photon interference theory, the probability of discovering two photons at the same position in the thermal field will be twice than that at different position [5], so the HBT effect is known as the photon bunching effect. However, comparing with the microscopic explanation, the macroscopic ones is that the auto-correlation of light intensity is inherently exceed the cross-correlation between different detected points in the detection plane with intensity fluctuations of thermal speckle [8]. According to statistical theory, the probability density function (PDF) of light intensity of thermal speckle follows a negative exponential distribution [9], so the second-order auto-correlation result is twice than that of cross-correlation ones.

In the traditional HBT effect with thermal light or pseudo-thermal light, the degree $\mathcal{D}^{(2)}$ of second-order coherence, i.e., peak-to-background ratio, is 2:1 [1, 10–12]. Researchers are actively exploring methods adopting classical light to increasing $\mathcal{D}^{(2)}$ and achieving

the super-bunching effect [13–28]. The realization of super-bunching effect with classical light holds significant promise for HBT-based applications, such as thermal light ghost imaging [29–35], sub-wavelength interference [36–38] and a high multi-photon effect but low average intensity [39], etc. In previous studies, researchers have introduced two primary strategies to increasing $\mathcal{D}^{(2)}$, manipulating the light source [13–18] and controlling the photon propagation [19–24]. For the former, the most representative approach involves introducing phase correlation into dynamic light source [13–15]. In contrast, the typical strategy of controlling photon propagation is using multiple incoherent two-photon paths [19–21]. While numerous research have been proposed to realize the super-bunching effect, projecting target pattern designed artificially onto the observation plane stands out because this is a simple and efficient strategy. For instance, dynamic patterns generated by digital micro-mirror devices (DMDs) are commonly transmitted onto the sample surface via the imaging lens in a single-pixel imaging scheme [40–43]. Consequently, the study on controlling the $g^{(2)}(0)$ peak value of bunching effect by optical projection with classical light is valuable.

In our work, we firstly conduct the theoretical analysis identifying key factors determining the $g^{(2)}(0)$ peak value of HBT effect of projection pattern in a single-lens incoherent imaging systems. And an efficient method estimating the $g^{(2)}(0)$ peak value by single-frame pattern is given. Then, we perform experimentally holographic projection in which target patterns originate from chaotic speckle and it's functional transformation. Corresponding projection results exhibit the active control the $g^{(2)}(0)$ peak value. What's more, we designed a set of sparse target patterns and demonstrated a strong

* liliming@sdut.edu.cn

super-bunching effect of holographic projection patterns. Finally, we confirm that holographic noise contributes to enhancing the $g^{(2)}(0)$ peak value of projection pattern.

II. THEORETICAL MODEL

Given that target patterns are typically digitized in the experiment, a discrete projection system is adopted in our theoretical analysis. For simplicity but without loss of generality, we present a detailed analytical derivation of the second-order spatial correlation function for the one-dimensional (1D) case in a single-lens incoherent imaging system with the image magnification factor of one. The extension to the two-dimensional (2D) scenario is straightforward and omitted here. If the κ th power of a dynamic thermal speckle $I_T(x, t)$ is taken as the target pattern, then the distribution of projection intensity $I_P(\xi, t)$ on imaging plane at the position ξ and the time t with a single-lens incoherent imaging system in the framework of the paraxial approximation satisfies:

$$I_P(\xi, t) = \sum_{\eta=1}^N I_T^\kappa(x_\eta, t) \text{somb}^2[k \text{NA}(\xi - x_\eta)], \quad (1)$$

$$\begin{aligned} g_P^{(2)}(\xi_1 = \xi_2 = \xi) &= \langle I_P^2(\xi, t) \rangle_t / \langle I_P(\xi, t) \rangle_t^2 \\ &= 1 + \frac{\sum_{\eta=1}^N \left(\text{somb}^2[k \text{NA}(\xi - x_\eta)] \sum_{\eta'=1}^N [g_T^{(2)}(x_\eta, x_{\eta'}) - 1] \cdot \text{somb}^2[k \text{NA}(\xi - x_{\eta'})] \right)}{\left(\sum_{\eta=1}^N \text{somb}^2[k \text{NA}(\xi - x_\eta)] \right)^2}, \end{aligned} \quad (3)$$

where $\langle \dots \rangle_t$ stands for the ensemble average over time t . The deduction of Eq. (3) is given in the appendix C. Note that, $g_P^{(2)}(\xi)$ is related to the target pattern and NA of projection system. It is not difficult to find that the maximum of $g_P^{(2)}(\xi)$ does not exceed $\mathcal{D}_\kappa^{(2)}$ and this discrepancy $g_P^{(2)}(\xi) - \mathcal{D}_\kappa^{(2)}$ diminishes as the NA increases.

To get the curve of normalized second-order correlation function of dynamic intensity patterns, we need intensity correlation of multi-frame sampling. However, if we only want to measure the peak value $g_P^{(2)}(\xi)$, the single-frame sampling is feasible with classical light because the result of ensemble average between in time t and in spatiality ξ are equivalent, i.e., $\langle I_P^2(\xi, t) \rangle_t = \langle I_P^2(\xi, t) \rangle_\xi$ and $\langle I_P(\xi, t) \rangle_t = \langle I_P(\xi, t) \rangle_\xi$. It stems from inherent properties of dynamic pattern: intensity of time series at a detected point will manifest somewhere in the detected plane at an arbitrary instant. What's more, if the boundaries of target pattern are infinite, $g_P^{(2)}(\xi)$ is independent of position ξ but the distance between two detected points (See Eq. (C7) for proof). Thus, the synchronous

where N is the number of total points of the target pattern, $\kappa \in \{0.5, 1, 2\}$ is the exponential term, $\text{somb}(x) = 2J_1(x)/x$ is the sombrero function, $k = 2\pi/\lambda$ is the wave vector of the wavelength λ , NA is the numerical aperture of the projection system, respectively. Here, $J_1(x)$ is the first-order Bessel function of the first kind.

In theory, the normal second-order spatial correlation function of target pattern $I_T^\kappa(x, t)$ can be expressed as:

$$g_T^{(2)}(x_\eta, x_{\eta'}) = 1 + (\mathcal{D}_\kappa^{(2)} - 1) \cdot \text{somb}^2[k \text{NA}'(x_{\eta'} - x_\eta)], \quad (2)$$

where $\mathcal{D}_\kappa^{(2)} = \mathbb{N}^{(2\kappa)} / (\mathbb{N}^{(\kappa)})^2$ is the degree of second-order coherence function of target pattern $I_T^\kappa(x, t)$ and NA' is the numerical aperture of experimental setup generated initial speckle $I_T(x, t)$. Here, $\mathbb{N}^{(\kappa)}$ is the degree of the κ th-order coherence function of speckle $I_T(x, t)$. Based on statistical property of thermal speckle, $\mathcal{D}_{\kappa=0.5}^{(2)}$, $\mathcal{D}_{\kappa=1}^{(2)}$ and $\mathcal{D}_{\kappa=2}^{(2)}$ are $4/\pi$, 2 and 6, respectively. In appendix, the Eq. (B2) provides a detailed description of $\mathbb{N}^{(\kappa)}$.

According to Eqs. (1)-(2) and the statistical theory, the synchronous-position second-order spatial correlation function at the projection plane can be expressed as:

position second-order spatial correlation function can be expressed as $g_P^{(2)}(0)$. It can be estimated as follow:

$$g_P^{(2)}(0) = \frac{D(I_P(\xi, t)) + E^2(I_P(\xi, t))}{E^2(I_P(\xi, t))}, \quad (4)$$

where the variance $D(I_P(\xi, t)) = \langle I_P^2(\xi, t) \rangle_\xi - \langle I_P(\xi, t) \rangle_\xi^2$ and the expectation $E(I_P(\xi, t)) = \langle I_P(\xi, t) \rangle_\xi$ can be calculated by a single-frame pattern, respectively.

III. EXPERIMENTAL VERIFICATION

Here, we adopt a holographic projection to demonstrate above theoretical analysis. Figure 1(a) shows the experimental setup of holographic projection to measure diffraction light intensity from a phase-only spatial light modulator (SLM, an element pixel size of $12.3 \times 12.3 \mu\text{m}^2$ and a total pixels 1280×1027 , GCI-770401, Daheng Optics, China). A single-mode continuous-wave laser beam with a wavelength $\lambda = 632.8 \text{ nm}$ was expanded, collimated and reshaped through a beam expander (BE) and

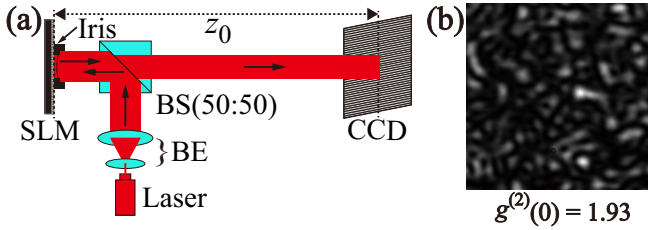


FIG. 1. (a) Schematic diagram of the experimental setup to measure diffraction light intensity from a phase-only spatial light modulator (SLM). BE: beam expander; BS: beam splitter; CCD: charge coupled device. (b) The single-frame experimental speckle from the chaotic source. The $g^{(2)}(0)$ peak value is 1.93 evaluated by using Eq. (4).

reflected by a 50:50 non-polarized beam splitter (BS). The reflected beam then immediately incident normally on the effective window of SLM. The phase-encoded laser beam successively transmits through the BS and be collected by a charge coupled device (CCD) camera. The distance z_0 between CCD and SLM is 54.6 cm. The experimental results detected by CCD camera are all far-field diffraction with an exposure time of 1.0 ms. Here, a lens phase factor $\exp\{-ikr_{\text{SLM}}^2/(2z_0)\}$ was superposed with the input diffraction phase factors. For a simplified description, the superposition of lens phase factors will not describe again. What's more, we can control the diffraction diameter D of effective window of SLM by a iris, which was placed as close as possible to the SLM.

Actually, target patterns of dynamic chaotic speckle sequences can be create in advance by the experimental setup of holographic projection as shown in Fig. 1(a). To create speckle sequence, a dynamic random phase factors $\exp\{i\phi(\vec{r}_{\text{SLM}}, t)\}$ puts into the SLM, where $\phi(\vec{r}_{\text{SLM}}, t) \in [0, 2\pi]$ is uniform distribution random phase codified onto the SLM and completely independent of spatiality and time. Figure 1(b) shows a single-frame experimental speckle with the diffraction diameter of chaotic source $D_{\text{chaotic}} = 4$ mm. According to Eq. (4), the $g^{(2)}(0)$ peak value of experimental speckle in Fig. 1(b) is 1.93 (displayed below the subgraph). The $g^{(2)}(0)$ evaluation by single-frame pattern using Eq. (4) is in good agreement with theoretical results $\mathcal{D}_{\kappa=1}^{(2)}$. Thus, the $g^{(2)}(0)$ evaluation by Eq. (4) will be widely adopted in our work.

To active control the $g^{(2)}(0)$ peak value, we employ two kinds of target patterns, chaotic speckle and sparse pattern, for the experimental investigation.

A. Chaotic speckle and it's function transformation patterns

Given that inevitable noise in the experimental data, we can obtained the simulated target pattern of noiseless chaotic speckle I_T according to the far-field diffraction of corresponding pre-established random phase via the Huygens-Fresnel (H-F) principle [44]. After the κ th

power of the chaotic speckle I_T , figures 2(a), 2(b) and 2(c) show those target patterns for the cases $\kappa = 0.5, 1$ and 2 from top to bottom, respectively. With the aid of Gerchberg-Saxton (GS) algorithm [45–47], we can obtain phase-only computer-generated holograms (CGHs) of those target patterns. Considering that phase retrieval by GS algorithm is prone to getting trapped in local optimum, we captured experimentally 1,000 projection results according to 1,000-frame CGHs by restart GS algorithm for individual target pattern. One of those 1,000 results is shown in Figs. 2(d), 2(e) and 2(f), respectively, corresponding target patterns in Figs. 2(a), 2(b) and 2(c), respectively. Here, the effective diameter D_{CGH} of CGH is 4 mm. Meanwhile, intensity average patterns of those 1,000 projection results are shown in Figs. 2(g), 2(h) and 2(i), respectively, corresponding target patterns in Figs. 2(a), 2(b) and 2(c), respectively. It is obvious that inevitable speckle noise in Figs. 2(d), 2(e) and 2(f) introduced by the coherence of laser beam during holographic projection can be greatly suppressed by average operation. Here, the $g^{(2)}(0)$ peak value of those target

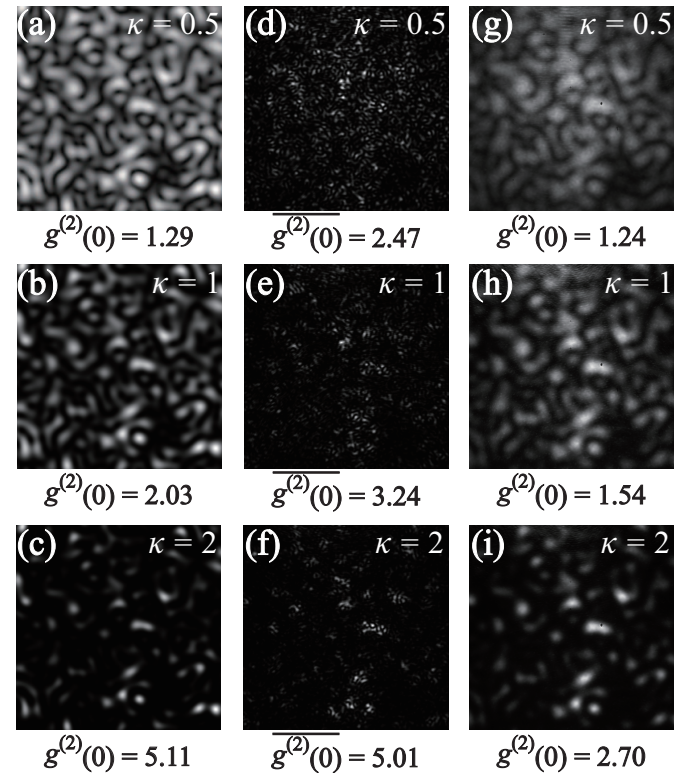


FIG. 2. Target patterns of chaotic speckle (a)-(c) and holographic projection patterns (d)-(i). Plotted is the κ th power of the simulated noiseless speckle for $\kappa = (a) 0.5, (b) 1$ and $(c) 2$, respectively. (d), (e) and (f) are one of 1,000 holographic projection results corresponding to target patterns in (a), (b) and (c), respectively. (g), (h) and (i) are the intensity average patterns of those 1,000 holographic projection results corresponding to target patterns in (a), (b) and (c), respectively. The evaluation of $g^{(2)}(0)$ peak value by using Eq. (4) is displayed below the subgraphs.

patterns in Figs. 2(a), 2(b) and 2(c) are 1.29, 2.03 and 5.11, respectively. Those results closely align with theoretical values $\mathcal{D}_\kappa^{(2)}$. For those single-frame holographic projection, we use the average peak value $g^{(2)}(0)$ of all projection results to evaluation. The average peak value $g^{(2)}(0)$ are 2.47, 3.24 and 5.01, respectively, corresponding target patterns in Figs. 2(a), 2(b) and 2(c), respectively. Interestingly, those projection results demonstrate the super-bunching characteristic, even if corresponding target patterns (the cases $\kappa = 0.5$ and 1) lack it. Here, the position of inevitable speckle noise, typically a drawback in holography reconstruction, is change from inferior to superior. In addition, the $g^{(2)}(0)$ peak value of those intensity average patterns in Figs. 2(g), 2(h) and 2(i) are 1.24, 1.54 and 2.70, respectively. As expected by Eq. (3), the $g^{(2)}(0)$ peak value of intensity average result of holographic projection will not be greater than the result of corresponding target pattern. What's more, after squaring operation at case $\kappa = 2$, the target pattern in Fig. 2(c) owns a broader dynamic range of light intensity so that the $g^{(2)}(0)$ peak value in Figs. 2(f) and 2(i) are affected dramatically by the environmental noise. Here, in order to better visualize the details of holographic projection, the subgraphs in Fig. 2 depict only the central

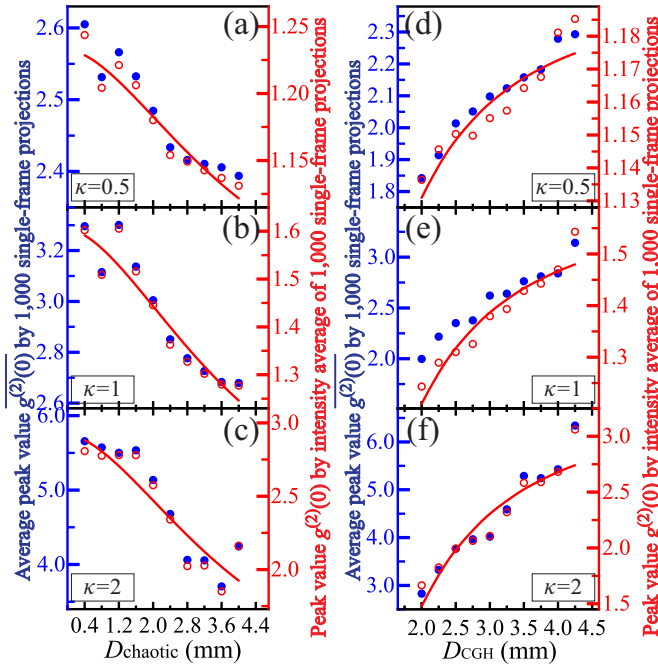


FIG. 3. Relationships between the $g^{(2)}(0)$ peak value and the chaotic source size D_{chaotic} for the cases $\kappa =$ (a) 0.5, (b) 1, and (c) 2 from top to bottom, respectively. Relationships between the $g^{(2)}(0)$ peak value and the CGH size D_{CGH} for the cases $\kappa =$ (d) 0.5, (e) 1, and (f) 2 from top to bottom, respectively. The blue solid circles are the average peak value $g^{(2)}(0)$ according to 1,000 projection pattern sequences. The red hollow circles are the $g^{(2)}(0)$ peak value for the intensity average pattern of these 1,000 frames projection results. The red solid curves are the theoretical linear fits by using Eq. (3).

regions of the original results.

Except for increasing the degree $\mathcal{D}^{(2)}$ of second-order coherence function of target pattern, there are two options that can enhance the $g^{(2)}(0)$ peak value of projection pattern according to Eq. (3). One is increasing the coherence length of the target pattern, and the other is improving NA of projection system. It is widely known that the coherence length of speckle is inversely proportional to the size of chaotic source [8]. By altering the size of chaotic source, a series of target chaotic speckle patterns can be obtained by the H-F principle. Maintaining the CGH's size $D_{\text{CGH}} = 4$ mm, holographic projection patterns corresponding those target patterns are acquired (no displayed here only estimated the $g^{(2)}(0)$ peak value by Eq. (4)). Figures 3(a), 3(b) and 3(c) shows the relationships between the $g^{(2)}(0)$ peak value and the size D_{chaotic} of chaotic source for the cases $\kappa = 0.5$, 1, and 2, respectively. The blue solid circles are the average peak value $g^{(2)}(0)$ according to 1,000 projection sequences for single target pattern. The red hollow circles are the peak value $g^{(2)}(0)$ for the intensity average of these 1,000 frames projection results. One notes that a larger size D_{chaotic} of chaotic source yield smaller coherence length leading to the fading of $g^{(2)}(0)$ peak value. Similarly, figures 3(d), 3(e) and 3(f) shows the relationships between the $g^{(2)}(0)$ peak value and the CGH's size D_{CGH} for the cases $\kappa = 0.5$, 1, and 2, respectively. Here, the size D_{chaotic} of chaotic source generating the target speckle pattern is 1 mm. As is well known that a fixed diffraction distance between the plane of CGH and the projection plane in the phase-only Fourier holography, a larger size of D_{CGH} corresponds to a larger NA [48] leading to a bigger the bunching peak value $g^{(2)}(0)$. In Fig. 3, the red solid curves are the theoretical linear fits by using Eq. (3). What's more, compared with those peak values originated from the intensity averaging by multi-frame projections, the single-frame holographic projection always shows a stronger $g^{(2)}(0)$ peak value.

To further verify the validity of the single-frame measurement method by Eq. (4), the $g^{(2)}(0)$ peak value results by the intensity correlation of multiple-frames patterns were compared. We captured experimentally holographic projection on 10,000 frames target patterns which originated from simulated noiseless chaotic speckle sequence. What's more, we collected experimentally the dynamic speckle sequence of chaotic source for comparative analysis. Figure 4 compares the measurement results of the $g^{(2)}(0)$ peak value between two methods: the intensity correlation by multi-frame patterns and the statistical analysis by single-frame pattern. Figure 4(a) shows the experimental results of the bunching effect by the multi-frame intensity correlation from chaotic source (black hollow circles) and three kinds of CGHs corresponding to speckle sequence of chaotic source after the power of $\kappa = 0.5$ (blue hollow squares), 1 (red hollow triangles), and 2 (green hollow diamonds), respectively. As expected, the $g^{(2)}(0)$ peak value of bunching effect with chaotic source is 1.88 which is close to theoretical

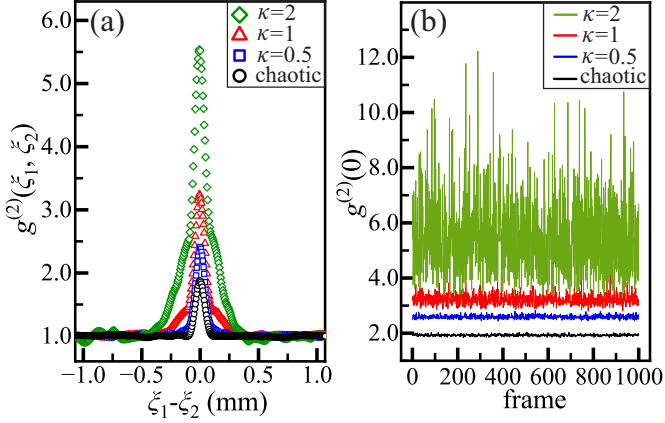


FIG. 4. Comparison of $g^{(2)}(0)$ peak value by two measurement methods: (a) the intensity correlation of multi-frame patterns and (b) the statistical analysis by single-frame pattern, respectively. (a) The second-order bunching effect calculated by 10,000 frames of chaotic speckles (black hollow circle) and holographic projection for the cases $\kappa = 0.5$, 1, and 2 (blue hollow squares, red hollow triangles, and green hollow diamonds, respectively). (b) Dynamic curves of $g^{(2)}(0)$ peak value taken over 1,000 frame of chaotic speckles (black line) and holographic projections corresponding to $\kappa = 0.5$, 1, and 2 (blue line, red line, and green line, respectively).

value $\mathcal{D}_{\kappa=1}^{(2)}$. Note that, those three kind of holographic projection show the super-bunching effect with bunching peak value 2.41, 3.24 and 5.54, respectively, corresponding to $\kappa = 0.5$, 1, and 2. What's more, those dynamic curves of the $g^{(2)}(0)$ peak value estimated by the statistical analysis of single-frame pattern by using Eq. (4) only on first 1,000 frames chaotic speckle (black line) and holographic projections corresponding to $\kappa = 0.5$, 1, and 2 (blue line, red line, and green line, respectively) are shown in Fig. 4(b). Since the data points on the curves in Fig. 4(b) is derived from distinct target pattern, the statistical analysis by single-frame pattern is influenced by the target pattern itself. Here, the average peak value $\overline{g^{(2)}(0)}$ of 10,000 frame patterns corresponding to chaotic speckle and holographic projection cases $\kappa = 0.5$, 1, and 2, are 1.94, 2.45, 3.09 and 5.27, respectively. It can be seen that those peak value results measured by two methods are essentially identical.

According to the above experimental results, a bigger the degree $\mathcal{D}^{(2)}$ of second-order coherence function of target pattern means a higher $g_P^{(2)}(0)$ peak value of the projection pattern. Therefore, holographic projection with sparse patterns artificially designed is studied in the following.

B. Sparse pattern

Figures 5 shows three kinds of 0-1 binary sparse target patterns and corresponding holographic projection patterns. To show details of holographic projection,

those results presented in Fig. 5 are only the central regions of original patterns. Here, those target patterns in Figs. 5(a), 5(b) and 5(c) are originated from all-zero matrix with a proportion $p = 1\%$, 0.5% and 0.1%, respectively, of 1 randomly inserted. Considering that those projection results of sparse patterns by GS-CGH exhibit better projection quality than the case of chaotic speckle, 100 restart GS projection results for a single-frame target pattern were experimentally captured. Figures 5(d), 5(e) and 5(f) are one of 100 holographic projection results corresponding to target patterns in Figs. 5(a), 5(b) and 5(c), respectively. What's more, figures 5(g), 5(h) and 5(i) are the patterns of intensity average of those 100 holographic projection results corresponding to target patterns in Figs. 5(a), 5(b) and 5(c), respectively. Here, the CGH's effective diameter D_{CGH} is 4 mm. The $g^{(2)}(0)$ peak value of those sparse target patterns in Figs. 5(a), 5(b) and 5(c) are 100.06, 199.81 and 992.98, respectively. Those results closely align with the theoretical two-order

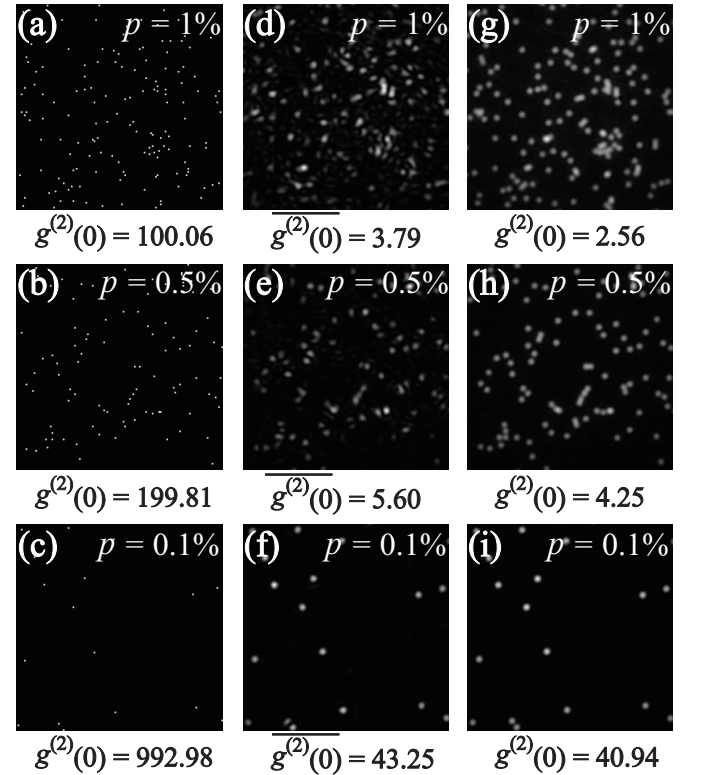


FIG. 5. 0-1 binary sparse target patterns (a)-(c) and holographic projection patterns (d)-(i). Sparse patterns originated from an all-zero matrix by inserting randomly 1 with a proportion of $p =$ (a) 1%, (b) 0.5% and (c) 0.1%, respectively. (d), (e) and (f) are one of 100 holographic projection results corresponding to target patterns in (a), (b) and (c), respectively. (g), (h) and (i) are the intensity average of those 100 holographic projection results corresponding to target patterns in (a), (b) and (c), respectively. The evaluation of $g^{(2)}(0)$ peak value by using Eq. (4) is displayed below the subgraphs.

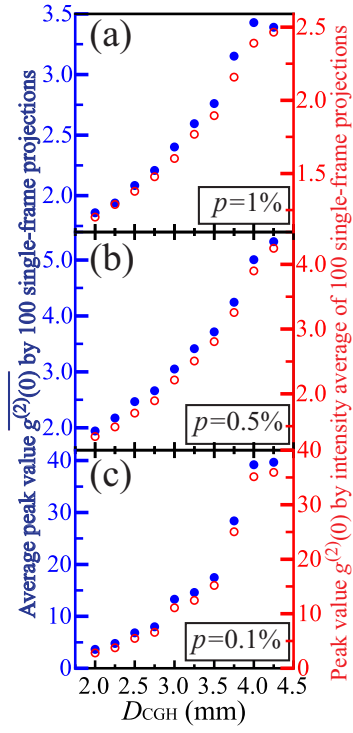


FIG. 6. Relationships between the $g^{(2)}(0)$ peak value and the CGH's size D_{CGH} with sparse patterns for the cases $p =$ (a) 1%, (b) 0.5%, and (c) 0.1% from top to bottom, respectively. The blue solid circles are the average peak value $\overline{g^{(2)}(0)}$ according to 100 projection pattern sequences. The red hollow circles are the $g^{(2)}(0)$ peak value for the intensity average pattern of these 100 projection results. Other experimental parameters are the same as those in Fig. 2(d).

degree $\mathcal{D}_p^{(2)} = 1/p$. For those 100 restart GS projections results, the average peak value $\overline{g^{(2)}(0)}$ are 3.79, 5.60 and 43.25, corresponding sparse target patterns in Figs. 5(a), 5(b) and 5(c), respectively. In addition, those peak value of projection patterns in Figs. 5(g), 5(h) and 5(i) by intensity average of those 100 projection results are decreased to 2.56, 4.25 and 40.94, respectively. It can be seen that the $g^{(2)}(0)$ peak value of single-frame projection outweighs that of multi-frame intensity averaging. However, the performance gap between two kinds of projection patterns gradually narrows along with sparsity of target pattern increasing.

To demonstrate the active control on the $g^{(2)}(0)$ peak value by the NA of holographic projection system with sparse patterns, figures 6(a), 6(b) and 6(c) shows the relationships between the $g^{(2)}(0)$ peak value and the CGH's size D_{CGH} with the cases $p = 1\%$, 0.5% , and 0.1% , respectively. Expect for the sampling quantity changed from 1,000 to 100, the rest of experimental parameters are the same as those in Fig. 2(d). As the size D_{CGH} of the CGH increases, the size of single bright granule in the projection pattern decreases. This results in a sparser intensity distribution, thus increasing the $g^{(2)}(0)$ peak value. It is consistent with the theoretical analysis

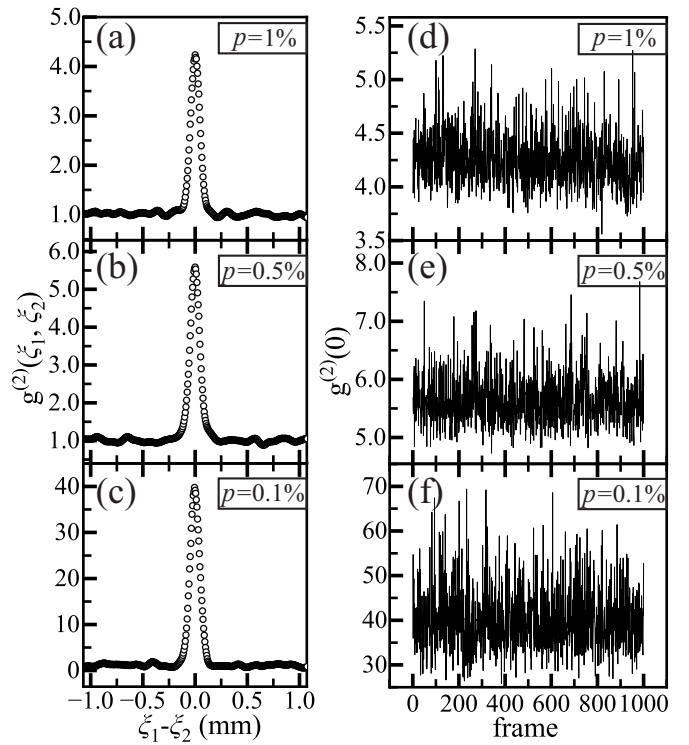


FIG. 7. Comparison of two measurement schemes on the $g^{(2)}(0)$ peak value by the intensity correlation of multi-frame patterns (a)-(c) and the statistical analysis by the single-frame pattern (d)-(f). The second-order bunching effect measured by the intensity correlation with 10,000 frames sparse projection patterns for the cases $p =$ (a) 1%, (b) 0.5%, and (c) 0.1% from top to bottom, respectively. (d)-(f) Dynamic curves of $g^{(2)}(0)$ peak value taken over first 1,000 single-frame holographic projections corresponding to $p = 1\%$, 0.5% , and 0.1% from top to bottom, respectively.

by Eq. (3).

To further identify the $g^{(2)}(0)$ peak value of the holographic projection by sparse patterns, figure 7 compares the measurement results by the intensity correlation method and the single-frame statistical analysis method. Figures 7(a), 7(b) and 7(c) shows the experimental results for the bunching effect by the 10,000-frame intensity correlation of projection patterns which originated from sparse patterns at the cases $p = 1\%$, 0.5% , and 0.1% , respectively. As the sparsity increases, the $g^{(2)}(0)$ peak values rises from 4.23 (the case $p = 1\%$) and 5.59 (the case $p = 0.5\%$) to 39.77 (the case $p = 0.1\%$). What's more, dynamic curves of the $g^{(2)}(0)$ peak value by single-frame evaluation only on first 1,000 holographic projection results are shown in Figs. 7(d), 7(e) and 7(f), corresponding to the cases $p = 1\%$, 0.5% , and 0.1% , respectively. Here, the average peak value $\overline{g^{(2)}(0)}$ of 10,000 frame patterns corresponding to cases $p = 1\%$, 0.5% , and 0.1% , are 4.24, 5.58 and 40.11, respectively. It can be seen that the single-frame evaluation method by Eq. (4) is effective and can be serve as a rapid prelim-

inary evaluation tool. In brief, the holographic projection demonstrates remarkably the strong super-bunching characteristics especially adopting sparse target patterns.

IV. DISCUSSION

Holographic projection is the combination of two optical systems, imaging and diffraction. In term of imaging, if the second-order coherence degree $\mathcal{D}^{(2)}$ of the light intensity on the object plane outweighs 2 meanwhile the spatial resolution of the imaging system reaches certain a threshold, the dynamic intensity on the imaging plane will exhibit the super-bunching effect according to Eq. (3). This has been confirmed by those results shown by red hollow circles in Figs. 3(d)-3(f) and Figs. 6(a)-6(c). Those results shown by red hollow circles are originated from the intensity average of multi-frame holographic projection pattern, which is similar like the point-to-point optical imaging. As we can seen, the improvement of spatial resolution of imaging system contributes to transfer the degree $\mathcal{D}^{(2)}$ of the target pattern to the imaging plane with less loss.

In addition, it is well-known that the speckle noise appears if the laser beam reflects from a rough surface [8, 49–52]. For example, the experimental speckle in Fig. 1(b) is originated from the far-field diffraction of coherent light wavefront modulated by a random phase. In our work, holographic projection is realized by the far-field diffraction of GS-CGH with a coherent light illumination. Thus, the speckle noise is a unavoidable defects for the holographic reconstruction but is profitable to enhancing the $g^{(2)}(0)$ peak value of projection pattern. In order to investigate the influence of speckle noise on the $g^{(2)}(0)$ peak value in a noise-free environment, we numerically simulated holographic projection by restart GS with all-one target pattern (no displayed here). Figure 8(a) is one of 10,000 holographic projection results according to restart GS algorithm. Here, the CGH's effective di-

ameter D_{CGH} is 4 mm. Other simulated parameters are same as those in Fig. 2(b). Figure 8(b) shows the second-order spatial correlation function calculated by intensity correlation according to those 10,000 frames holographic projection. Here, the speckle noise originated from the holographic projection shows the bunching effect with the full width at half maximum (FWHM) $89.1 \mu\text{m}$ and the peak value 2.00 of bunching effect. What's more, dynamic curves of the $g^{(2)}(0)$ peak value only on first 1,000 holographic projection results is shown in Fig. 8(c). Here, the average peak value $\overline{g^{(2)}(0)}$ of 1,000 holographic projection is 1.99. Note that, the FWHM of the bunching peak represents the average size of speckle grains and the $g^{(2)}(0)$ peak value lies with PDF of light intensity of speckle noise. Furthermore, dynamic curves of the $g^{(2)}(0)$ peak value in Fig. 8(c) demonstrates that each speckle pattern of 10,000 holographic projection exhibits identical statistically behavior. According to the similar result of bunching effect and dynamic curves of $g^{(2)}(0)$ peak value of chaotic light speckle in Fig. 4, those two types of speckle (chaotic speckle and speckle noise of holographic projection) exhibit identical physical properties.

Except for target pattern, the speckle noise of holographic projection will secondarily modulate the statistical distribution of projection pattern leading to increasing the $g^{(2)}(0)$ peak value. Thus, the $g^{(2)}(0)$ peak value of holographic projection pattern can be effectively controlled through three categories: the degree and coherent length of target pattern, the number of intensity average of projection pattern, and the physical size of the CGH in holographic projection.

V. CONCLUSION

We theoretically established the relationship of normalized second-order correlation functions between the object plane and image plane in a single-lens incoherent imaging system, thereby enabling theoretical prediction of the bunching peak value at the image plane. Furthermore, an efficient evaluation method for bunching peak values is proposed using a single-frame speckle pattern, which is then applied to subsequent experimental measurements. Experimentally, both chaotic speckle and sparse pattern based on GS-CGH are employed to validate the theoretical analysis. Here, a super-bunching effect with $g^{(2)}(0) = 39.77$ is realized by holographic projection in which the target pattern is artificially designed sparse pattern. Additionally, we demonstrate that the speckle noise of holographic projection increases the the $g^{(2)}(0)$ peak value of HBT effect.

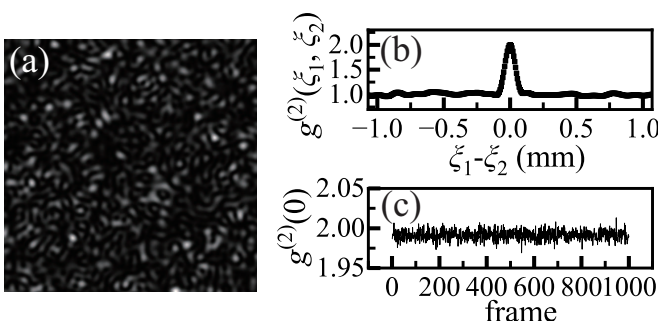


FIG. 8. (a) Noise speckle in holographic projection with a all-one target pattern. (b) The second-order bunching effect measured with 10,000 frames intensity correlation by restart GS algorithm for the all-one target. (c) Dynamic curves of peak value $g^{(2)}(0)$ taken over first 1000 holographic projections.

ACKNOWLEDGMENTS

This work was supported by the NSFC (Grant No. 62105188).

Appendix A: The expected value of a random variable

Type one: X is a discrete random variable.

$$E(X) = \sum_{i=1}^{\infty} X_i p_i(X = X_i), \quad (\text{A1})$$

where p_i is the probability that X is equal to X_i .

Type two: X is a continuous random variable.

$$E(X) = \int_{-\infty}^{+\infty} x f_X(x) dx, \quad (\text{A2})$$

where $f_X(x)$ is PDF of random variable X .

Type three: a random variable $Z = g_1(X)$ is a function of the random variable X . Here, $g_1(X)$ is known. According to the type of the random variable X , the expected value of Z can be expressed as [53]:

$$E(Z) = \sum_{i=1}^{\infty} g_1(X_i) p_i(X = X_i), \quad (\text{A3})$$

or

$$E(Z) = \int_{-\infty}^{+\infty} g_1(x) f_X(x) dx. \quad (\text{A4})$$

Type four: a random variable $Z = g_2(X, Y)$ is a function of two random variables X and Y . Similarly, the function $g_2(X, Y)$ is known and the expected value of Z can be expressed as [53]:

$$E(Z) = \sum_{i=1}^{\infty} \sum_{j=1}^{\infty} g_2(X_i, Y_j) p_i(X = X_i) p_j(Y = Y_j), \quad (\text{A5})$$

or

$$E(Z) = \int_{-\infty}^{+\infty} \int_{-\infty}^{+\infty} g_2(x, y) f_{(X, Y)}(x, y) dx dy. \quad (\text{A6})$$

Here, $f_{(X, Y)}(x, y)$ is the joint PDF of variables X and Y .

Appendix B: The expected value of dynamic speckle and it's power transformation of thermal source

For dynamic speckle pattern $I_T(x, t)$, the PDF [9] is

$$f_{I_T}(i_T) = \frac{1}{\bar{I}_T} \exp\left(-\frac{i_T}{\bar{I}_T}\right), \quad (\text{B1})$$

where $i_T > 0$ and $\bar{I}_T = \langle I_T(x, t) \rangle_t$ is the expected value over t at any point on the target plane. According to Eqs. (A4) and (B1), the expected value of $I_T^\kappa(x, t)$, the κ th power of thermal speckle, can be expressed as:

$$\langle I_T^\kappa(x, t) \rangle_t = \int_0^{+\infty} i_T^\kappa f_{I_T}(i_T) di_T = \aleph^{(\kappa)} \bar{I}_T^\kappa, \quad (\text{B2})$$

where $\aleph^{(\kappa)}$ is the degree of the κ th-order coherence function of dynamic thermal speckle. When κ is an integer, the degree satisfies $\aleph^{(\kappa)} = N!$. Interestingly, this result is also valid at $\kappa = \frac{1}{2}$. According to the generalized factorial [54], the degree of the $\frac{1}{2}$ th-order coherence function of thermal speckle satisfies $\aleph^{(\frac{1}{2})} = \frac{1}{2}! = \frac{\sqrt{\pi}}{2}$.

Appendix C: The expected value of projection pattern with a single-lens incoherent imaging system

According to Eqs. (1), (A4), (B1) and (B2), the expected value of intensity distribution of projection pattern at the position ξ can be expressed as:

$$\langle I_P(\xi, t) \rangle_t = \sum_{\eta=1}^N \aleph^{(\kappa)} \bar{I}_T^\kappa \times \text{somb}^2 [kNA(\xi - x_\eta)]. \quad (\text{C1})$$

For the expected value of the product of the projection pattern of two detection points, we generalize it from special to general. If there is an effect correlation only within adjacent ± 1 points on target pattern, the product of light intensity can be expressed as:

$$\begin{aligned} & I_P(\xi_1, t) I_P(\xi_2, t) \\ &= \sum_{\eta_1=1}^N I_T^\kappa(x_{\eta_1}, t) \text{somb}^2 [kNA(\xi_1 - x_{\eta_1})] \\ & \quad \times \sum_{\eta_2=1}^N I_T^\kappa(x_{\eta_2}, t) \text{somb}^2 [kNA(\xi_2 - x_{\eta_2})] \\ &= \mathcal{P}_1 + \mathcal{P}_2, \end{aligned} \quad (\text{C2})$$

with $\eta_1 \neq \{\eta_2, \eta_2 \pm 1\}$ case

$$\begin{aligned} \mathcal{P}_1 &= \sum_{\eta_1=1}^N I_T^\kappa(x_{\eta_1}, t) \text{somb}^2 [kNA(\xi_1 - x_{\eta_1})] \\ & \quad \times \sum_{\eta_2=1}^N I_T^\kappa(x_{\eta_2}, t) \text{somb}^2 [kNA(\xi_2 - x_{\eta_2})] \\ & \quad \times (1 - \delta_{\eta_1, \eta_2} - \delta_{\eta_1, \eta_2+1} - \delta_{\eta_1, \eta_2-1}), \end{aligned} \quad (\text{C3})$$

and $\eta_1 = \{\eta_2, \eta_2 \pm 1\}$ case

$$\begin{aligned} \mathcal{P}_2 &= \sum_{\eta_1=1}^N I_T^\kappa(x_{\eta_1}, t) \text{somb}^2 [kNA(\xi_1 - x_{\eta_1})] \\ & \quad \times \sum_{\eta_2=1}^N I_T^\kappa(x_{\eta_2}, t) \text{somb}^2 [kNA(\xi_2 - x_{\eta_2})] \\ & \quad \times (\delta_{\eta_1, \eta_2} + \delta_{\eta_1, \eta_2+1} + \delta_{\eta_1, \eta_2-1}). \end{aligned} \quad (\text{C4})$$

As we can see, $I_P(\xi_1, t) I_P(\xi_2, t)$ is divided into two parts \mathcal{P}_1 and \mathcal{P}_2 , which are originated from a function of two random variables $I_T^\kappa(x_{\eta_1}, t)$ and $I_T^\kappa(x_{\eta_2}, t)$. In \mathcal{P}_1 , these two random variables are completely independent, but they are not in \mathcal{P}_2 . According to Eqs. (A6), (B1) and (B2), the ensemble average of $I_P(\xi_1, t) I_P(\xi_2, t)$ can be expressed as:

$$\begin{aligned}
\langle I_P(\xi_1, t) I_P(\xi_2, t) \rangle_t &= \langle \mathcal{P}_1 \rangle_t + \langle \mathcal{P}_2 \rangle_t \\
&= (\mathfrak{N}^{(\kappa)})^2 \bar{I}_T^{2\kappa} \sum_{\eta_1=1}^N \text{somb}^2 [k\text{NA}(\xi_1 - x_{\eta_1})] \sum_{\eta_2=1}^N \text{somb}^2 [k\text{NA}(\xi_2 - x_{\eta_2})] \\
&\quad - (\mathfrak{N}^{(\kappa)})^2 \bar{I}_T^{2\kappa} \sum_{\eta=1}^N \text{somb}^2 [k\text{NA}(\xi_1 - x_{\eta})] \text{somb}^2 [k\text{NA}(\xi_2 - x_{\eta})] \\
&\quad - (\mathfrak{N}^{(\kappa)})^2 \bar{I}_T^{2\kappa} \sum_{\eta=1}^N \text{somb}^2 [k\text{NA}(\xi_1 - x_{\eta})] \text{somb}^2 [k\text{NA}(\xi_2 - x_{\eta} + \Delta_x)] \\
&\quad - (\mathfrak{N}^{(\kappa)})^2 \bar{I}_T^{2\kappa} \sum_{\eta=1}^N \text{somb}^2 [k\text{NA}(\xi_1 - x_{\eta})] \text{somb}^2 [k\text{NA}(\xi_2 - x_{\eta} - \Delta_x)] \\
&\quad + (\mathfrak{N}^{(\kappa)})^2 g_T^{(2)}(0) \bar{I}_T^{2\kappa} \sum_{\eta=1}^N \text{somb}^2 [k\text{NA}(\xi_1 - x_{\eta})] \text{somb}^2 [k\text{NA}(\xi_2 - x_{\eta})], \\
&\quad + (\mathfrak{N}^{(\kappa)})^2 g_T^{(2)}(-\Delta_x) \bar{I}_T^{2\kappa} \sum_{\eta=1}^N \text{somb}^2 [k\text{NA}(\xi_1 - x_{\eta})] \text{somb}^2 [k\text{NA}(\xi_2 - x_{\eta} + \Delta_x)] \\
&\quad + (\mathfrak{N}^{(\kappa)})^2 g_T^{(2)}(\Delta_x) \bar{I}_T^{2\kappa} \sum_{\eta=1}^N \text{somb}^2 [k\text{NA}(\xi_1 - x_{\eta})] \text{somb}^2 [k\text{NA}(\xi_2 - x_{\eta} - \Delta_x)].
\end{aligned} \tag{C5}$$

In fact, the dynamic light intensity correlation between different detected points (or two random variables $I_T^\kappa(x_{\eta_1}, t)$ and $I_T^\kappa(x_{\eta_2}, t)$) in the target plane can be ex-

pressed by Eq. (2). Thus, the normal second-order spatial correlation function at the projection plane can be expressed as:

$$\begin{aligned}
g_P^{(2)}(\xi_1, \xi_2) &= \frac{\langle I_P(\xi_1, t) I_P(\xi_2, t) \rangle_t}{\langle I_P(\xi_1, t) \rangle_t \langle I_P(\xi_2, t) \rangle_t} \\
&= 1 + \frac{\sum_{\eta=1}^N \left(\text{somb}^2 [k\text{NA}(\xi_1 - x_{\eta})] \sum_{\eta'=1}^N [g_T^{(2)}(x_{\eta}, x_{\eta'}) - 1] \times \text{somb}^2 [k\text{NA}(\xi_2 - x_{\eta'})] \right)}{\left(\sum_{\eta=1}^N \text{somb}^2 [k\text{NA}(\xi_1 - x_{\eta})] \right) \left(\sum_{\eta=1}^N \text{somb}^2 [k\text{NA}(\xi_2 - x_{\eta})] \right)}.
\end{aligned} \tag{C6}$$

For continuous systems with an infinitely extended object plane, the corresponding expression of Eq. (C6) is:

$$g_P^{(2)}(\xi_1, \xi_2) = 1 + \frac{\iint \text{somb}^2(k\text{NA}x_{\eta}) \text{somb}^2(k\text{NA}x_{\eta'}) [g_T^{(2)}(x_{\eta} - x_{\eta'} + \xi_1 - \xi_2) - 1] dx_{\eta} dx_{\eta'}}{\left(\int \text{somb}^2(k\text{NA}x_{\eta}) dx_{\eta} \right)^2}. \tag{C7}$$

Note that, $g_P^{(2)}(\xi_1, \xi_2)$ is independent of single point position ξ but the distance $\xi_1 - \xi_2$ between two detected points. This means that the bunching effect of the pro-

jected pattern satisfies the space translation invariance, which is one of the necessary conditions for ghost imaging [35, 44].

[1] R. H. Brown and R. Q. Twiss, Correlation between photons in two coherent beams of light, *Nature* **177**, 27 (1956).
[2] R. H. Brown and R. Q. Twiss, A test of a new type of

stellar interferometer on sirius, *Nature* **178**, 1046 (1956).
[3] I. Silva and O. Freire Jr., The concept of the photon in question: The controversy surrounding the HBT effect circa 1956–1958,

Historical Studies in the Natural Sciences **43**, 453 (2013).

[4] M. Born and E. Wolf, *Principles of Optics* (Elsevier, 2013).

[5] M. O. Scully and M. S. Zubairy, *Quantum Optics* (Cambridge University Press, 1997).

[6] R. Loudon, *The Quantum Theory of Light* (OUP Oxford, 2000).

[7] Y. Shih, *An Introduction to Quantum Optics: Photon and Biphoton Physics* (CRC Press, 2011).

[8] J. W. Goodman, *Speckle Phenomena in Optics: Theory and Applications* (Roberts and Company Publishers, 2007).

[9] J. W. Goodman, Some fundamental properties of speckle, *Journal of the Optical Society of America* **66**, 1145 (1976).

[10] Y. Zhou, J. Simon, J. Liu, and Y. Shih, Third-order correlation function and ghost imaging of chaotic thermal light in the photon counting regime, *Physical Review A* **81**, 043831 (2010).

[11] J. Liu and Y. Shih, Nth-order coherence of thermal light, *Physical Review A* **79**, 023819 (2009).

[12] L. Li, P. Hong, and G. Zhang, Transverse revival and fractional revival of the Hanbury Brown and Twiss bunching effect with discrete chaotic light, *Physical Review A* **99**, 023848 (2019).

[13] Y. Bromberg and H. Cao, Generating non-Rayleigh speckles with tailored intensity statistics, *Physical Review Letters* **112**, 213904 (2014).

[14] R. Liu, B. Qing, S. Zhao, P. Zhang, H. Gao, S. Chen, and F. Li, Generation of non-Rayleigh nondiffracting speckles, *Physical Review Letters* **127**, 180601 (2021).

[15] S. Han, N. Bender, and H. Cao, Tailoring 3D speckle statistics, *Physical Review Letters* **130**, 093802 (2023).

[16] B. Chen, J. Yuan, X. Li, X. Peng, and B. Sun, High-speed generation of non-Rayleigh speckle, *Optics Express* **32**, 11952 (2024).

[17] Y. Zhou, X. Zhang, Z. Wang, F. Zhang, H. Chen, H. Zheng, J. Liu, F.-L. Li, and Z. Xu, Superbunching pseudothermal light with intensity modulated laser light and rotating groundglass, *Optics Communications* **437**, 330 (2019).

[18] J. Liu, R. Zhuang, X. Zhang, C. Wei, H. Zheng, Y. Zhou, H. Chen, Y. He, and Z. Xu, Simple and efficient way to generate superbunching pseudothermal light, *Optics Communications* **498**, 127264 (2021).

[19] P. Hong, J. Liu, and G. Zhang, Two-photon superbunching of thermal light via multiple two-photon path interference, *Physical Review A* **86**, 013807 (2012).

[20] Y. Zhou, F.-L. Li, B. Bai, H. Chen, J. Liu, Z. Xu, and H. Zheng, Superbunching pseudothermal light, *Physical Review A* **95**, 053809 (2017).

[21] L. Zhang, Y. Lu, D. Zhou, H. Zhang, L. Li, and G. Zhang, Superbunching effect of classical light with a digitally designed spatially phase-correlated wave front, *Physical Review A* **99**, 063827 (2019).

[22] Y. Zhou, S. Luo, Z. Tang, H. Zheng, H. Chen, J. Liu, F.-L. Li, and Z. Xu, Experimental observation of three-photon superbunching with classical light in a linear system, *Journal of the Optical Society of America B* **36**, 96 (2019).

[23] S. Luo, H. Zheng, W. Xu, Y. He, S. Zhang, J. Tian, and Z. Xu, Temporal and spatial superbunching effects from a pair of modulated distinguishable classical lights, *Journal of the Optical Society of America B* **38**, 2148 (2021).

[24] S. Luo, Y. Zhou, H. Zheng, J. Liu, H. Chen, Y. He, W. Xu, S. Zhang, F. Li, and Z. Xu, Two-photon superbunching effect of broadband chaotic light at the femtosecond timescale based on a cascaded Michelson interferometer, *Physical Review A* **103**, 013723 (2021).

[25] S. Zhang, H. Zheng, G. Wang, J. Liu, S. Luo, Y. He, Y. Zhou, H. Chen, and Z. Xu, Controllable superbunching effect from four-wave mixing process in atomic vapor, *Optics Express* **28**, 21489 (2020).

[26] Z. Ye, H.-B. Wang, J. Xiong, and K. Wang, Antibunching and superbunching photon correlations in pseudo-natural light, *Photonics Research* **10**, 668 (2022).

[27] C.-Q. Wei, J.-B. Liu, X.-X. Zhang, R. Zhuang, Y. Zhou, H. Chen, Y.-C. He, H.-B. Zheng, and Z. Xu, Non-Rayleigh photon statistics of superbunching pseudothermal light, *Chinese Physics B* **31**, 024209 (2022).

[28] Y. Dong, J. Liu, Z. Xi, H. Zhang, Y. Sun, K. Yu, Y. Liu, and Z. Xu, Physics of bunching and superbunching in superbunching pseudothermal light, *Journal of the Optical Society of America B* **41**, 1599 (2024).

[29] R. S. Bennink, S. J. Bentley, R. W. Boyd, and J. C. Howell, Quantum and classical coincidence imaging, *Physical Review Letters* **92**, 033601 (2004).

[30] A. Gatti, E. Brambilla, M. Bache, and L. A. Luigato, Ghost imaging with thermal light: Comparing entanglement and classical correlation, *Physical Review Letters* **93**, 093602 (2004).

[31] A. Valencia, G. Scarcelli, M. D'Angelo, and Y. Shih, Two-photon imaging with thermal light, *Physical Review Letters* **94**, 063601 (2005).

[32] I. N. Agafonov, M. V. Chekhova, T. S. Iskhakov, and A. N. Penin, High-visibility multiphoton interference of Hanbury Brown-Twiss type for classical light, *Physical Review A* **77**, 053801 (2008).

[33] K. W. C. Chan, M. N. O'Sullivan, and R. W. Boyd, High-order thermal ghost imaging, *Optics Letters* **34**, 3343 (2009).

[34] J. Gateau, T. Chaigne, O. Katz, S. Gigan, and E. Bossy, Improving visibility in photoacoustic imaging using dynamic speckle illumination, *Optics Letters* **38**, 5188 (2013).

[35] X. Wu, Y. Zhao, and L. Li, High-visibility ghost imaging with phase-controlled discrete classical light sources, *Chinese Physics B* **33**, 074202 (2024).

[36] J. Xiong, D.-Z. Cao, F. Huang, H.-G. Li, X.-J. Sun, and K. Wang, Experimental observation of classical subwavelength interference with a pseudothermal light source, *Physical Review Letters* **94**, 173601 (2005).

[37] P. Hong and G. Zhang, Subwavelength interference with an effective entangled source, *Physical Review A* **88**, 043838 (2013).

[38] Y. Zhai, F. E. Becerra, J. Fan, and A. Migdall, Direct measurement of sub-wavelength interference using thermal light and photon-number-resolved detection, *Applied Physics Letters* **105**, 101104 (2014).

[39] K. Y. Spasibko, D. A. Kopylov, V. L. Krutyanskiy, T. V. Murzina, G. Leuchs, and M. V. Chekhova, Multiphoton effects enhanced due to ultrafast photon-number fluctuations, *Physical Review Letters* **119**, 223603 (2017).

[40] M. F. Duarte, M. A. Davenport, D. Takhar, J. N. Laska, T. Sun, K. F. Kelly, and R. G. Baraniuk, Single-pixel imaging via compressive sampling, *IEEE Signal Processing Magazine* **25**, 83 (2008).

[41] M. P. Edgar, G. M. Gibson, and M. J. Padgett, Principles and prospects for single-pixel imaging,

[Nature photonics](#) **13**, 13 (2019).

[42] G. M. Gibson, S. D. Johnson, and M. J. Padgett, Single-pixel imaging 12 years on: a review, [Optics Express](#) **28**, 28190 (2020).

[43] K. Song, Y. Bian, D. Wang, R. Li, K. Wu, H. Liu, C. Qin, J. Hu, and L. Xiao, Advances and challenges of single-pixel imaging based on deep learning, [Laser & Photonics Reviews](#) **19**, 2401397 (2025).

[44] J. W. Goodman, *Introduction to Fourier Optics* (McGraw-Hill, New York, 1995).

[45] R. W. Gerchberg and W. O. Saxton, A practical algorithm for the determination of phase from image and diffraction plane pictures, [Optik](#) **35**, 237 (1972).

[46] K. Liu, Z. He, and L. Cao, Double amplitude freedom Gerchberg–Saxton algorithm for generation of phase-only hologram with speckle suppression, [Applied Physics Letters](#) **120**, 061103 (2022).

[47] D. Zhou, L. Zhang, H. Zhang, and G. Zhang, Ghost images with controllable visibility and spatial resolution, [Optics Express](#) **31**, 14659 (2023).

[48] J. W. Goodman, An introduction to the principles and applications of holography, [Proceedings of the IEEE](#) **59**, 1292 (1971).

[49] L. I. Goldfischer, Autocorrelation function and power spectral density of laser-produced speckle patterns, [Journal of the Optical Society of America](#) **55**, 247 (1965).

[50] J. C. Dainty, *Laser Speckle and Related Phenomena*, Vol. 9 (Springer science & business Media, 2013).

[51] A. Gatti, D. Magatti, and F. Ferri, Three-dimensional coherence of light speckles: Theory, [Physical Review A](#) **78**, 063806 (2008).

[52] D. Magatti, A. Gatti, and F. Ferri, Three-dimensional coherence of light speckles: Experiment, [Physical Review A](#) **79**, 053831 (2009).

[53] A. Leon-Garcia, *Probability, Statistics, and Random Processes for Electrical Engineering* (Pearson Education, 2017).

[54] M. Bhargava, The factorial function and generalizations, [The American Mathematical Monthly](#) **107**, 783 (2000).